



### Science Arts & Métiers (SAM)

is an open access repository that collects the work of Arts et Métiers Institute of Technology researchers and makes it freely available over the web where possible.

This is an author-deposited version published in: <https://sam.ensam.eu>  
Handle ID: <http://hdl.handle.net/10985/21500>

#### To cite this version :

Abderezak AOUALI, Stéphane CHEVALIER, Alain SOMMIER, M. AYADI, Jean-Christophe BATSALE, Daniel BALAGEAS, Christophe PRADERE - Ultra-broadband contactless imaging power meter - Applied Optics - Vol. 60, n°26, p.7995 - 2021

Any correspondence concerning this service should be sent to the repository

Administrator : [scienceouverte@ensam.eu](mailto:scienceouverte@ensam.eu)



# Ultra-broadband contactless imaging power meter

A. AOUALI,<sup>1,\*</sup> S. CHEVALIER,<sup>2</sup> A. SOMMIER,<sup>1</sup> M. AYADI,<sup>2</sup> J.-C. BATSALE,<sup>2</sup> D. BALAGEAS,<sup>1</sup> AND C. PRADERE<sup>1</sup>

<sup>1</sup>I2M TREFLE, UMR 5295 CNRS-UB-ENSAM, 351 Cours de la Libération, 33400 Talence, France

<sup>2</sup>Arts et Métiers Institute of Technology, Université de Bordeaux, CNRS, INRA, INP, I2M, HESAM. Esplanade des arts et métiers, F-33400 Talence, France

\*Corresponding author: abderezak.aouali@u-bordeaux.fr

Received 1 June 2021; revised 30 July 2021; accepted 4 August 2021; posted 6 August 2021 (Doc. ID 432479); published 0 MONTH 0000

**Knowledge of the spatial and temporal distribution of heat flux is of great interest for the quantification of heat sources. In this work, we describe the development of a new ultra-broadband contactless imaging power meter based on electromagnetic to infrared technology. This new sensor and the mathematical processing of images enable the reconstruction of both spatial and amplitude distributions through a wide spectral range of sources. The full modeling of the thermoconverter based on 3D formalism of thermal quadrupoles is presented first before deriving a reduced model more suitable for quick and robust inverse processing. The inverse method makes it possible to simultaneously identify the heat losses and the spatial and temporal source distribution for the first time, to the best of our knowledge. Finally, measurements of multispectral sources are presented and discussed, with an emphasis on the spatial and temporal resolution, accuracy and capabilities of the power meter.** © 2021 Optical Society of America

<https://doi.org/10.1364/AO.432479>

## Nomenclature

$A$	Absorbance
$T$	Temperature in real space, K
$\hat{\theta}$	Temperature in the cosine transformed space
$\theta$	Temperature in cosine and Laplace transformed space
$h_c$	Convective exchange coefficient, $\text{W m}^{-2} \text{K}^{-1}$
$\hat{h}$	Source point impulse response in real space
$H$	Source point impulse response in cosine and Laplace transformed space
$\hat{H}$	Source point impulse response in cosine transformed space
$\hat{H}^\ominus$	Source point Heaviside response in cosine transformed space
$\mathcal{Y}$	Internal source in real space, $\text{W m}^{-3}$
$Y$	Internal source in cosine and Laplace transformed space
$\delta$	Dirac function
$\Theta$	Heaviside function
$\lambda$	Thermal conductivity, $\text{W m}^{-1} \text{K}^{-1}$
$a$	Thermal diffusivity, $\text{m}^2 \text{s}^{-1}$
$\rho$	Mass density, $\text{kg m}^{-3}$
$C_p$	Specific heat, $\text{J K}^{-1} \text{kg}^{-1}$
$\phi_0, \phi_e$	Excitation flux in boundary condition (respectively, input and output fluxes), $\text{W m}^{-2}$
$e$	Thickness of the thermoconverter, $m$

$L$	Lateral dimension of the thermoconverter, m
$t$	Time, s
$x, y, z$	Spatial coordinates
$Z_j^i$	Thermal impedance in Laplace and cosine transform space, $i$
layer number, $j$	Thermal impedance number
$\nabla$	Laplacian

## 1. INTRODUCTION

The development of imaging sensors to measure radiative heat flux has attracted a considerable amount of attention in the research community in recent years. Whereas many works have focused on imaging sensors for visible light [1–4], few tools exist for other wavelength ranges, particularly the millimeter to meter range [5,6]. Knowledge of the heat flux generated by a multispectral source is of prime interest in numerous experimental setups, i.e., in building sciences, aeronautic industries, optical applications, and heat transfer. A quantitative image of radiative heat flux (or thermal source) would enable the performance of heat balance to serve as input data for models or to control online processes. In this context, the development of a new sensor implies, first, developing the hardware (the component sensitive to the heat excitation) and, second, determining the

(Table continued)

36 mathematical modeling of the hardware response to obtain  
37 quantitative data.

38 There are two main types of flux sensors: thermal and pho-  
39 tonic sensors. Photonic sensors are based on the photoelectric  
40 effect and are predominantly used at higher frequencies in the  
41 visible, ultraviolet, and X-ray spectral ranges [7]. In contrast,  
42 thermal detectors are mainly used at longer wavelengths [5,6].  
43 In this study, the choice of hardware is based on the electro-  
44 magnetic infrared (EMIR) technology developed by Balageas  
45 *et al.* [8]. In their work, Balageas *et al.* reported a hyperspectral  
46 sensor using a very thin and homogeneous carbon film called  
47 a hyperspectral thermoconverter. This device has the ability to  
48 absorb radiation over a very wide spectral range (from visible  
49 to radio waves) with different sensitivities (depending on the  
50 wavelength) [5,9]. Electromagnetic waves are absorbed by the  
51 carbon film and converted into heat, which is transported by  
52 conduction in the thin film before being re-emitted as infrared  
53 (IR) light. Thus, this carbon thermoconverter enables imaging  
54 of ultra-broadband heat flux when used in combination with  
55 an IR camera. However, before obtaining a quantitative image  
56 of the heat flux or the thermal source detected by the sensor,  
57 thorough mathematical processing based on thermal inverse  
58 methods is required.

59 Depending on the nature of the heat transfer, i.e., conduc-  
60 tion, convection, or radiation, there are several methods for  
61 estimating the heat source [10–12]. In the present study, the  
62 reconstruction of the heat fields is essentially based on the  
63 knowledge of conductive transfer. Garderein *et al.* [13] devel-  
64 oped a point sensor system based on a thermocouple to estimate  
65 local fluxes by analytical inverse thermal methods. Another  
66 study from Zeribi *et al.* [14] reported the fabrication of a 2D  
67 non-imaging heat flux sensor based on the spatial temperature  
68 gradient method. Image reconstruction was addressed by Groz  
69 *et al.* [15,16], who reported a method to reconstruct deep heat  
70 sources using analytical models and two inversion methods  
71 (statistical and deconvolution by Toeplitz). Another 3D recon-  
72 struction method was recently developed by Burgholzer *et al.*  
73 [17,18]. This method combines IR thermography and the con-  
74 cept of virtual waves. However, in these studies, the quantitative  
75 goal of estimating the heat flux amplitude was not achieved  
76 because the location of the sources is assumed to be unknown.  
77 Finally, Nortershauser *et al.* [19,20] addressed the development  
78 of a source reconstruction method (spatial distribution and flux  
79 amplitude) using numerical models for inversion. The con-  
80 straint of this method is mainly related to the calculation time.  
81 However, the authors proposed the use of a statistical estimator  
82 in the cosine transformed space to reduce the calculation time.

83 From all of these seminal works, it was demonstrated that both  
84 quantitation and spatial distribution of the heat flux are needed  
85 to process the images formed on a thermal thermoconverter.  
86 Such a quantitative method combined with the EMIR technol-  
87 ogy will enable the development of new electromagnetic sensors  
88 to reconstruct both spatial and amplitude distributions over  
89 a wide spectral range by passing through cosine transformed  
90 space. Indeed, this passage through cosine transformed space is  
91 of considerable interest when calculating convolution products  
92 and results in a substantial advantage in terms of calculation  
93 time.

94 The present work reports the development of an ultra-  
95 broadband contactless imaging power meter. To the best of our  
96 knowledge, such a hyperspectral sensor allowing the measure-  
97 ment of thermal flux images and the reconstruction of the source  
98 has not previously been reported in the literature. To address  
99 this objective, the thermophysical properties of the hardware,  
100 i.e., the thermoconverter associated with a research-grade IR  
101 camera, are thoroughly characterized. The method used for  
102 mathematical processing of the images formed on the thermo-  
103 converter is then presented. Finally, several examples at various  
104 wavelengths [from near-IR (NIR) to radio waves] are presented  
105 and discussed. The limits and accuracy of these new sensors are  
106 also discussed at the end of the paper.

## 2. EXPERIMENTAL SETUP

107 The experimental setup is described in a general manner in  
108 Fig. 1. A multispectral source is used to optically illuminate  
109 and heat the thermoconverter by the photothermal effect.  
110 The heat absorption depends on the wavelength. For example,  
111 the absorbance is 100% in the NIR to far-IR range and only  
112 61% in the millimeter range [9]. Heating the film increases its  
113 thermal radiative emission, which is detected by an IR camera.  
114 The camera used is an InSb SC 7000 from FLIR [working in  
115 the spectral range (1.5–5.5  $\mu\text{m}$ ) with  $240 \times 320$  pixels and a  
116 pitch size of  $25 \mu\text{m} \times 25 \mu\text{m}$ , this camera will be used for all  
117 powermeter applications] placed behind the thermoconverter  
118 (in this IR band, the thermoconverter can be assimilated to a  
119 blackbody  $\epsilon \approx 1$  [9]). This photon-phonon-photon conversion  
120 has the advantage of being ultra-broadband and the drawback  
121 of not having enough power to sufficiently heat the converter to  
122 achieve acceptable IR camera sensitivity.  
123

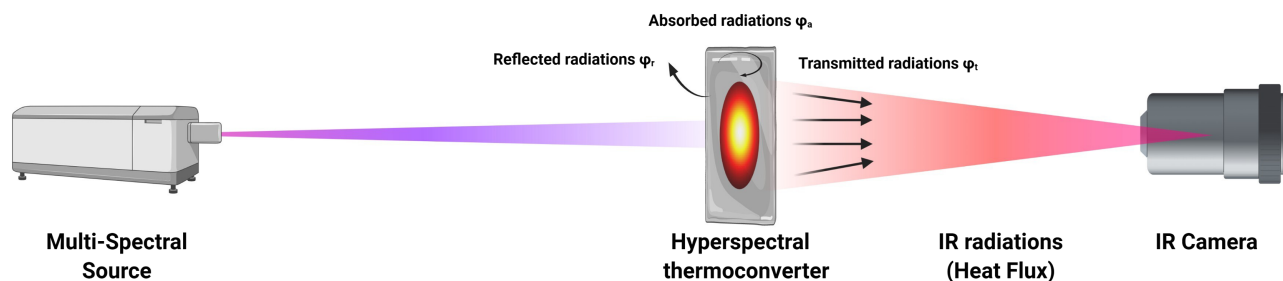


Fig. 1. Schema of the experimental setup.

124  
125  
126  
127  
128  
129  
130  
131  
132  
133  
134  
135  
136  
137  
138  
139  
140  
141  
142  
143  
144  
145

### 3. MODELING HEAT TRANSFER IN THE THERMOCONVERTER

#### A. Complete Thermal Model of the Thermoconverter

The thermoconverter can be considered a thin homogeneous medium (a thermally thin body due to its small thickness,  $L = 5 \text{ cm}$  and  $e = 37 \mu\text{m}$ ) subjected to convective/radiative heat loss and containing an internal heat source. Due to the very large ratio between the lateral dimensions and the thickness ( $L \gg e$ ), the temperature gradient across the thickness of the thermoconverter is neglected. Thus, it is advisable to consider the surrounding environment [21]. The influence of the air around the thermoconverter is not negligible and considerably affects the temperature of the thermoconverter. This can be explained by the presence of effusive exchanges between the thermoconverter (thermally thin body) and the surrounding environment. Therefore, the analytical model that accurately describes the heat transfer in the thermoconverter must include the surrounding layers. In Fig. 2, there are three layers: air-thermoconverter-air. The evolution of the temperature fields in the system described in Fig. 2 is determined by the three-layer 3D heat conduction equation with an internal volume source located in the thermoconverter layer:

$$\left\{ \begin{array}{l} \frac{1}{a_r} \frac{\partial T_r(x, y, z, t)}{\partial t} - \frac{1}{\lambda_{r=2}} \mathcal{D}_{r=2}(x, y, z, t) - \nabla^2 T_r(x, y, z, t) = 0, \quad r = 1, 2, 3, \\ -\lambda_r \frac{\partial T_r(x, y, z, t)}{\partial x} \Big|_{x=\pm \frac{L_x}{2}} = 0, \quad -\lambda_r \frac{\partial T_r(x, y, z, t)}{\partial y} \Big|_{y=\pm \frac{L_y}{2}} = 0, \\ \lambda_{r=1} \frac{\partial T_{r=1}(x, y, z, t)}{\partial z} \Big|_{z=j} = -\lambda_{r=2} \frac{\partial T_{r=2}(x, y, z, t)}{\partial z} \Big|_{z=j} = -h_c T_{r=2}(x, y, z = j, t), \\ -\lambda_{r=2} \frac{\partial T_{r=2}(x, y, z, t)}{\partial z} \Big|_{z=k} = \lambda_{r=3} \frac{\partial T_{r=3}(x, y, z, t)}{\partial z} \Big|_{z=k} = h_c T_{r=2}(x, y, z = k, t), \\ T_{r=1}(x, y, z = j, t) = T_{r=2}(x, y, z = j, t), \\ T_{r=2}(x, y, z = k, t) = T_{r=3}(x, y, z = k, t), \\ T_r(x, y, z, t = 0) = 0, \end{array} \right. \quad (1)$$

146 where  $r$  is the layer number, i.e., 1 for air, 2 for the thermocon-  
147 verter, and 3 for air, as depicted in Fig. 2.

#### B. Assumptions and Solution

148 In this part, the solution of the three-layer system is described.  
149 This solution is based on the 3D formalism of thermal  
150 quadrupoles [22,23] using the transformed impedances in  
151

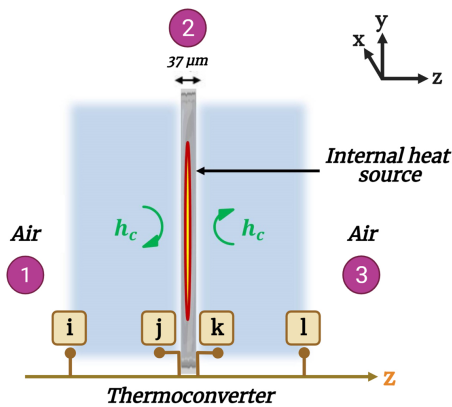


**Fig. 2.** Complete thermal model of the thermoconverter (i, l, physical boundary of the air layers; j, k, plans of the interfaces between the thermoconverter and the air layers).

cosine Laplace spaces. The equivalent electrical network of the system is shown in Fig. 3(a), in which each layer is composed of three impedances. In this case, it is considered that the contact between the layers is perfect (no contact thermal resistance between the layers), and the internal source is uniformly distributed through the entire thickness of the thermoconverter. To solve the three-layer system, the following assumptions are made:

- Adiabatic boundary conditions on each side of layers 1 and 3: the impedances  $Z_1^1$  of layer 1 and  $Z_2^3$  of layer 3 are neglected [Fig. 3(b)] because the interest is focused only on the energy contribution of the internal heat source, as shown in Fig. 2 (absence of  $\phi_0$  and  $\phi_e$ ).
- Semi-infinite medium configuration: the purpose of choosing a three-layer system as a model is to take into account the influences of adjacent media (mainly air) on the thermoconverter, so the impedances  $Z_3^3$  and  $Z_2^1$  of layer 1 and the impedances  $Z_1^3$  and  $Z_3^3$  of layer 3 are replaced by two semi-infinite impedances,  $Z_\infty^1$  and  $Z_\infty^3$ , respectively [Fig. 3(c)].
- Thermally thin body: the thermoconverter was previously described as a thermally thin body (no temperature gradient in

the thickness). This leads to the suppression of the impedances  $Z_1^{\text{th}}$  and  $Z_2^{\text{th}}$ , and only the impedance  $Z_3^{\text{th}}$  is necessary to evaluate the temperature of the thermoconverter [Fig. 3(d)].

Figure 3 shows the reduction steps according to the assumptions made, as well as the equivalent electrical networks obtained at each step. Based on the electric current conservation law at the node of the thermoconverter layer in Fig. 3(d), the temperature expression of the thermoconverter in the Laplace cosine transformed space is written as follows:

$$\theta_{\text{Th}} = \left( \frac{1}{Z_{\text{eq}}^1} + \frac{1}{Z_{\text{Th}}^3} + \frac{1}{Z_{\text{eq}}^3} \right)^{-1} \times Y, \quad (2)$$

with

$$Z_{\text{eq}}^{1,3} = \left( b + \frac{1}{Z_\infty^{1,3}} \right)^{-1}, \quad \text{where } Z_\infty^{1,3} = (\lambda\gamma)^{-1} \quad \text{and} \quad \gamma = \sqrt{\frac{p}{a} + \alpha_n^2 + \beta_m^2}. \quad (3)$$

The capacitive impedance of the thermoconverter is written as follows:

152  
153  
154  
155  
156  
157  
158  
159  
160  
161  
162  
163  
164  
165  
166  
167  
168  
169  
170  
171  
172  
173  
174

175  
176  
177  
178  
179  
180  
181  
182  
183  
184

185

186  
187

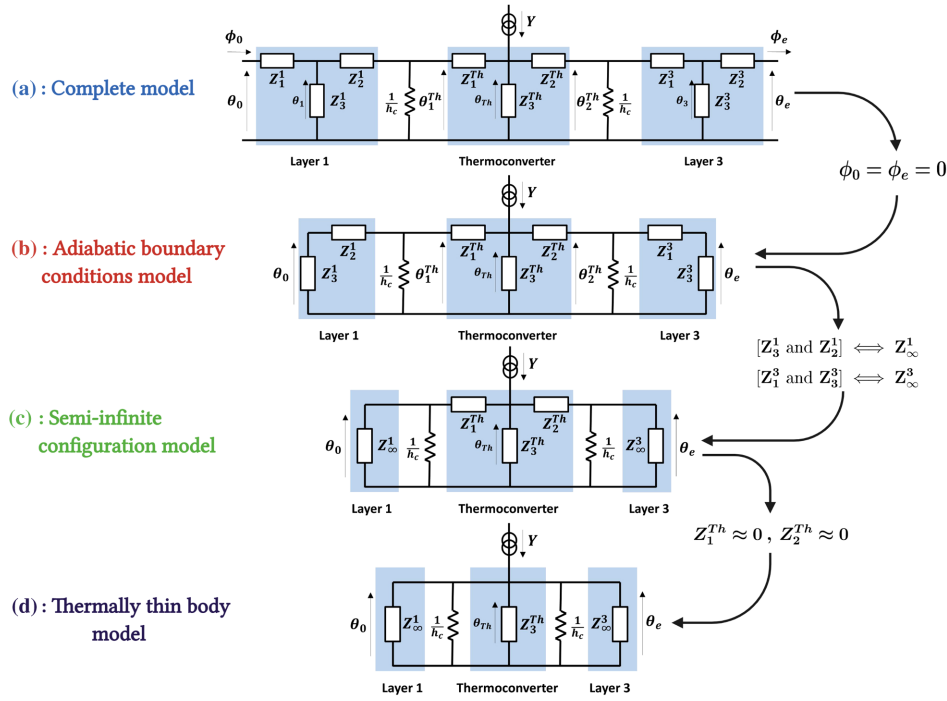


**Fig. 3.** Reduction steps of the thermoconverter model: (a) complete model, (b) adiabatic boundary conditions model, (c) semi-infinite configuration model, and (d) thermally thin body model.

$$Z_3^{Th} = (\lambda \gamma \sinh(\gamma \ell))^{-1}, \quad \text{where } \gamma = \sqrt{\frac{p}{a} + \alpha_n^2 + \beta_m^2}, \quad (4)$$

where  $\alpha_n = n\pi/L_x$ ,  $n \in \mathbb{N}$  and  $\beta_m = m\pi/L_y$ ,  $m \in \mathbb{N}$  represent the spatial frequencies, and  $p$  represents the Laplace variable.  $Y$  represents the internal source in Laplace cosine transformed space, it is written as

$$Y(\alpha_n, \beta_m, p) = \int_0^{+\infty} \int_0^{L_x} \int_0^{L_y} \mathcal{Y}(x, y, t) \times \exp(-pt) \cos(\alpha_n x) \cos(\beta_m y) dt dx dy. \quad (5)$$

Finally, the temperature of the thermoconverter in the Laplace cosine transformed space is obtained as

$$\theta_{Th}(\alpha_n, \beta_m, p) = \int_0^{+\infty} \int_0^{L_x} \int_0^{L_y} T_{Th}(x, y, t) \times \exp(-pt) \cos(\alpha_n x) \cos(\beta_m y) dt dx dy. \quad (6)$$

Equation (2) can be rewritten simply as follows:

$$\theta_{Th}(\alpha_n, \beta_m, p) = H(\alpha_n, \beta_m, p) \times Y(\alpha_n, \beta_m, p),$$

$$H(\alpha_n, \beta_m, p) = \left( \frac{1}{Z_{eq}^1} + \frac{1}{Z_3^{Th}} + \frac{1}{Z_{eq}^3} \right)^{-1}. \quad (7)$$

To compute the spatial temperature field, one inverse Laplace in time [24] and two inverse cosine transformations are necessary.

**Table 1.** Thermophysical Properties of the Different Layers Given in Ref. [26] for Air

	Air	Thermoconverter
Thickness (m)	$\infty$	$37 \pm 1 \times 10^{-6}$
$\lambda$ ( $\text{W m}^{-1} \text{K}^{-1}$ )	0.026	$1.414 \pm 0.041$
$\rho C_p$ ( $\text{J K}^{-1} \text{m}^{-3}$ )	1313	$2.83 \pm 0.03 \times 10^6$
$a$ ( $\text{m}^2 \text{s}^{-1}$ )	$1.98 \times 10^{-5}$	$5.0 \pm 0.1 \times 10^{-7}$

All of the parameters of the thermoconverter needed for the construction of the model have been estimated. The thickness measured by a micrometer was  $37 \pm 1 \mu\text{m}$ . The thermal diffusivity was estimated by the flying spot technique [25] to be  $a = 5.0 \pm 0.1 \times 10^{-7} \text{m}^2 \cdot \text{s}^{-1}$ . Using conventional thermal characterization techniques, the remaining thermophysical properties of the thermoconverter were measured: (i) the density was calculated by means of a helium pycnometer to be  $\rho = 1800 \pm 10 \text{kg} \cdot \text{m}^{-3}$ , and (ii) the specific heat was estimated by a Setaram 131 differential scanning calorimeter to be  $C_p = 1572 \pm 8 \text{J} \cdot \text{K}^{-1} \cdot \text{kg}^{-1}$ .

The thermophysical properties of air were obtained from the literature [26] (see Table 1).

### C. Validation of the Assumptions

Two studies have been carried out, as described in this section, to validate the assumptions made previously. The first study consists of a comparison between the temperature fields of the thermoconverter calculated by means of the four different models described in Fig. 3. The spatial shape of the source used is concentric circles, and a Dirac pulse  $\delta(t)$  was used for temporal excitation. The value of the heat loss was set to

198  
199  
200  
201  
202  
203  
204  
205  
206  
207  
208  
209  
210

211  
212  
213  
214  
215  
216  
217  
218

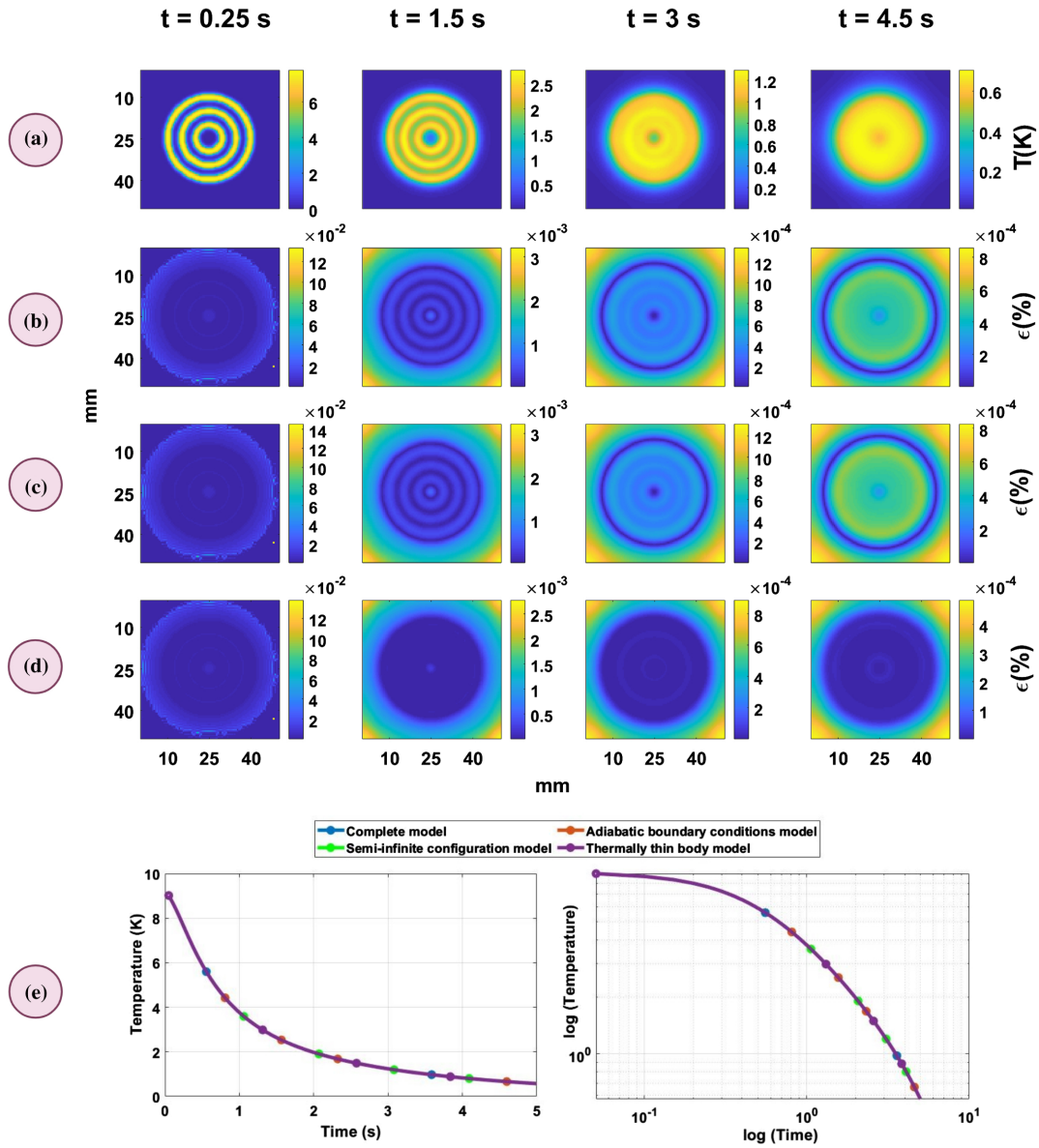


**Fig. 4.** Comparison of the temperature determined by the four models: (a) diffusion of the source obtained by the complete model, (b) calculated error (in %) between the source diffusion obtained from the complete model and that obtained from the adiabatic boundary conditions model, (c) calculated error (in %) between the source diffusion obtained from the complete model and that obtained from the semi-infinite configuration model, (d) calculated error (in %) between the source diffusion obtained from the complete model and that obtained from the thermally thin body model, and (e) diffusion of one pixel versus time determined by the four models.

219  $h_c = 20 \text{ W} \cdot \text{m}^{-2} \cdot \text{K}^{-1}$ . This study allows the validation of  
 220 the reduction steps of the model. The second study consists  
 221 of generating a flux balance using the model to calculate the  
 222 rate of heat flux dissipated in each impedance that constitutes  
 223 the system. This second study allows quantitative evaluation  
 224 of the heat transfer mechanism contribution and the effect of  
 225 considering the air layers in the model.

226 It can be seen from Fig. 4 that the temperature fields of the  
 227 thermoconverter are quasi-identical for the four different mod-  
 228 els. Figure 4(e) confirms the previous finding by showing that  
 229 the transient heat transport is also identical for the different  
 230 models. This effectively enables the validation the different  
 231 assumptions described in Section 3.B.

232 Figure 5 illustrates the flux balance. Figure 5(a) shows the rate  
 233 of the transient heat flux (delivered by the internal source) dissi-  
 234 pated by the volume of the thermoconverter, air, and convective  
 235 heat loss. Figure 5(b) shows the sum of all of the fluxes, which  
 236 must be equal to 100% at all times (conservation of energy). In  
 237 Fig. 5(a), we can see that at short times ( $t < 2$  s) the influence  
 238 of the air layers appears very early and is important enough to  
 239 be neglected (5% at  $t = 0.17$  s, 10% at  $t = 0.8$  s). Moreover,  
 240 the heat flux dissipated by convective heat loss intervenes later  
 241 than the air (5% at  $t = 1$  s, 10% at  $t = 2$  s) to then reach a more  
 242 important rate at long times (35% at  $t = 10$  s). In conclu-  
 243 sion, it should be noted that the dissipation of the flux in the  
 244 semi-infinite impedances of the air occurs rapidly and is quite

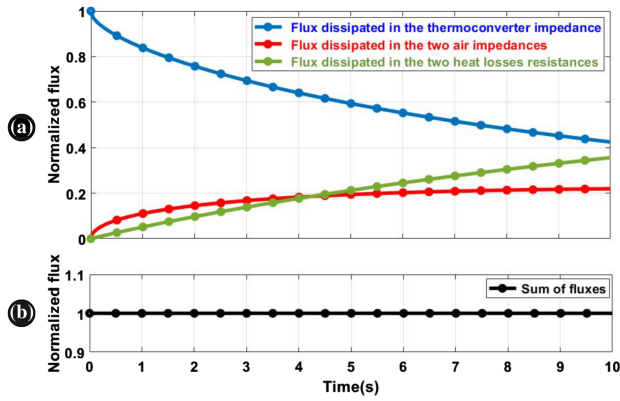


Fig. 5. Heat flux balance.

important. This proves that the consideration of the environment around the thermoconverter in the model is primordial. It should also be noted that the dissipation of the flux through the heat loss resistances occurs less rapidly over time and is also important. Therefore, it is necessary to estimate the heat losses to form a complete model.

#### 4. INVERSE METHOD DESCRIPTION

##### A. Inverse Method for Source Estimation

Based on Eq. (7), the output temperature can simply be written as a space–time convolution product of the source and the impulse response of the source point:

$$T_{\text{Th}}(x, y, t) = \mathcal{Y}(x, y, t) \otimes \hat{h}(x, y, t), \quad (8)$$

where  $\hat{h}(x, y, t)$  is the impulse response in real space–time. The source  $\mathcal{Y}(x, y, t)$  can be decomposed into a product of a spatial function  $\mathcal{F}(x, y)$ , amplitude  $\mathcal{Y}_0$ , and a temporal function  $\Theta(t)$ . After passing through the space transformed cosine base, only the temporal convolution remains. In the case of a Heaviside-type temporal excitation and after applying the Laplace transform on time, we have

$$\theta_{\text{Th}}(\alpha_n, \beta_m, p) = \mathcal{Y}_0 \times \hat{\mathcal{F}}(\alpha_n, \beta_m) \times \underbrace{\left[ \frac{1}{p} \times H(\alpha_n, \beta_m, p) \right]}_{H^\ominus}, \quad (9)$$

where  $H^\ominus$  represents the response of the source point to the Heaviside temporal excitation in Laplace cosine transformed space. By applying the Laplace inverse transform to Eq. (9), the source can be estimated in the cosine transformed space via the following relation:

$$\mathcal{Y}_0 \times \hat{\mathcal{F}}(\alpha_n, \beta_m) = \hat{\theta}_{\text{Th}}(\alpha_n, \beta_m, t) \times \left[ \hat{H}^\ominus(\alpha_n, \beta_m, t) \right]^{-1}. \quad (10)$$

Inverse thermal problems are known to be ill-posed problems [27]. This is essentially due to the condition of instability of the solution obtained by inversion. To remedy this condition, the inversion is carried out by constructing a Wiener filter. This filter is based on Tikhonov’s regularization method [28], which is used and applied in the Cosine transformed space as follows:

$$\mathcal{Y}_0 \times \hat{\mathcal{F}}(\alpha_n, \beta_m) = \hat{\theta}_{\text{Th}}(\alpha_n, \beta_m, t) \times \frac{\hat{H}^\ominus(\alpha_n, \beta_m, t)}{|\hat{H}^\ominus(\alpha_n, \beta_m, t)|^2 + \mu |\hat{D}(\alpha_n, \beta_m)|^2}, \quad (11)$$

where  $D$  is a derivation matrix [29] in the cosine transformed space, and  $\mu$  is the regularization coefficient [30]. In the end, to retrieve the spatial distribution of the source, two inverse cosine transformations are necessary.

##### B. Heat Losses Estimation

As shown in Section 3.C, the heat losses by convection need to be measured along with the spatial distribution of the source in order to adapt to the external environment. Thus, based on the fact that the spatial average of a 3D temperature field leads to the one-dimensional (1D) temperature field [22] and the fact that the relaxation of the temperature field due to a Heaviside excitation corresponds to a response to an amplified Dirac excitation, a method of heat loss estimation based on a linear least-squares minimization between the normalized spatial average of the relaxation experimental temperature field (see Fig. 6) and the normalized spatial average of temperature field obtained from the model Eq. (2) (for a Dirac time excitation) is described in this section.

Assuming that the measured temperature field of the thermoconverter is  $T_{\text{mes}}(x, y, t)$ , the spatial average of this temperature field is calculated for each time step and normalized by its maximum to arrive at  $\tilde{T}_{\text{mes}}^*(t)$ .

Then, a variable change over time is applied,  $t^* = t - t_0$ , where  $t_0$  corresponds to the time of the beginning of relaxation ( $\tilde{T}_{\text{mes}}^*(t_0) = 1$ ); this new time base  $t^*$  is used to calculate the numerical temperature field of the thermoconverter (for a Dirac time excitation) from the model described in Section 3.B for different values of  $h_c$ . The temperature field obtained is spatially averaged and then normalized by its maximum to obtain the following:  $\tilde{T}_{\text{model}}^*(t^*)$ .

Finally, the minimization is achieved using the Nelder–Mead simplex method [31],

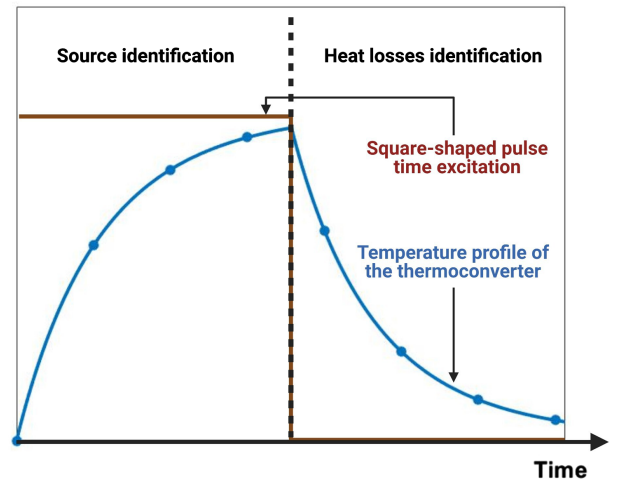


Fig. 6. Square-shaped pulse time excitation to be used for the estimation of the heat losses as well as the heat source.

**Table 2. Thermophysical Properties of the Foam [32,33]**

	Thickness (m)	$\lambda$ ( $\text{W m}^{-1} \text{K}^{-1}$ )	$\rho C_p$ ( $\text{J K}^{-1} \text{m}^{-3}$ )	$a$ ( $\text{m}^2 \text{s}^{-1}$ )
Foam	$\infty$	0.03	47600	$6.3 \times 10^{-7}$

$$h_{\text{estimated}} = \operatorname{argmin} \left\{ \left\| \bar{T}_{\text{model}}^*(t^*, h) - \bar{T}_{\text{mes}}^*(t^*) \right\|^2 \right\}. \quad (12)$$

### C. Optimization of the Experimental Process for Estimation

To simultaneously and continuously estimate the convective heat loss and the excitation flux of the source, a square-shaped pulse is used for temporal excitation of the internal source. Figure 6 shows the square-shaped pulse time excitation as well as the temperature profile of the thermoconverter in the presence of the resulting heat losses. The choice of square-shaped pulse time excitation is justified by the fact that there is a constant level where the internal source is switched on (temperature rise of the thermoconverter), which is used to identify the source, and another constant level where the internal source is switched off (relaxation of the thermoconverter), which is used to estimate the heat loss. The estimation of the heat loss makes it possible to reintroduce this loss into the model described in Section 3.B and thus makes it complete.

## 5. RESULTS AND DISCUSSION

### A. Contact Validation by Joule Effect

One of the most robust ways to control the power dissipated by a source is to use an electrical resistance heated by the Joule effect. This is used to validate the method of reconstruction of the source. To do this, a complex-shaped resistance with an internal ohmic resistance of  $73\Omega$  is used. The setup used is described in Fig. 7(a). An electrical current generator supplied the resistance during 1.5 s. The voltage is verified at the edge of the resistance by a voltmeter to be  $U = 4.93$  V. This theoretically corresponds to the dissipation of a power equal to  $P = 333$  mW. The thermoconverter is attached on the resistor, which is insulated by foam (polyurethane foam). Finally, an IR camera is used for the acquisitions.

In this case, only the parameters of the model to be used for the inversion are modified. The proposed model allows changing the parameters easily to match the real experimental configuration. One of the semi-infinite impedances of the air is then replaced by a semi-infinite impedance of the insulated foam, and the heat loss by convection is neglected on this side.

Figure 7(b) shows the normalized spatial average of the measured 3D temperature field. This field allows the identification of the  $t_0$  and the construction of the new time base  $t^*$ , which is used to estimate the heat loss. Figure 7(c) shows the result of the minimization described in Section 4.B, and the convective exchange coefficient is estimated to be  $4.53 \pm 0.3 \text{ W} \cdot \text{m}^{-2} \cdot \text{K}^{-1}$ . The estimated value of this coefficient is coherent, given that one side of the thermoconverter is insulated by the foam, and the average increase in the temperature is low (on the order of 0.4 K at  $t = 1$  s).

Figures 8(a) and 8(b) show the reconstruction of the spatial distribution and power density of the source after inversion.

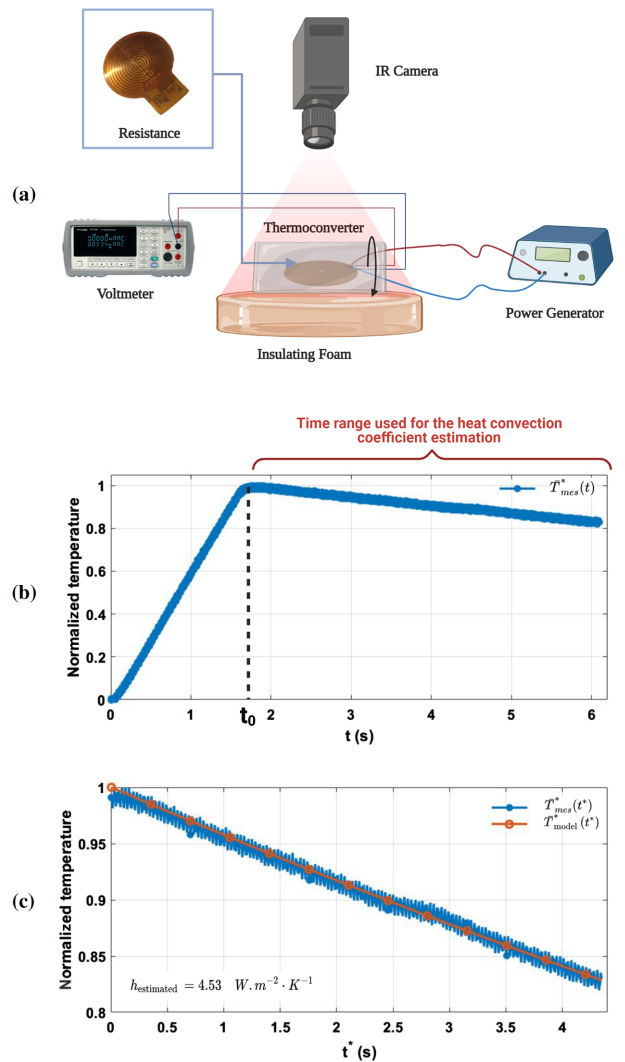


**Fig. 7.** (a) Experimental setup, (b) normalized spatial average of the 3D temperature field measured, and (c) comparison between the experimental data and the model using  $h_c = 4.53 \text{ W} \cdot \text{m}^{-2} \cdot \text{K}^{-1}$ .

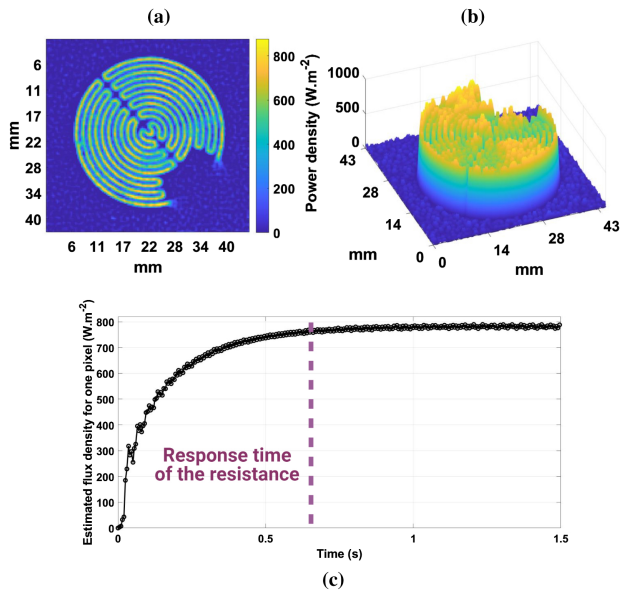
It can be observed here that the spatial distribution of the estimated source fits well with the shape of the resistance presented in Fig. 7(a). Nevertheless, the spatial repartition of the flux is not uniform over the entire surface of the resistance, which can be explained by small adhesion defects between the thermoconverter and the resistance.

Figure 8(c) shows the reconstruction of the flux density for a single pixel over time. It can be seen that the flux density increases progressively (transient state) due to the inertia of the resistance (volumetric source) before reaching a constant level (steady state), which represents the real power density dissipated by the Joule effect.

Two methods exist to determine the injected flux: (i) multiplying the flux density imaged by the area and then integrating it or (ii) integrating the flux density image and multiplying the result by the area of one pixel. By applying the first method and considering that the absorbance of the thermoconverter in the IR is almost 100% [9], we obtain

$$P_{\text{estimated}} = \left( \oint \mathcal{Y}(x, y) \right) \times S_{\text{pixel}} = 331.5 \pm 1.9 \text{ mW}, \quad (13)$$

354  
355  
356  
357  
358  
359  
360  
361  
362  
363  
364  
365  
366  
367  
368  
369  
370  
371



**Fig. 8.** (a) Image of the estimated source, (b) surface of the estimated source, and (c) estimated flux density for one pixel.

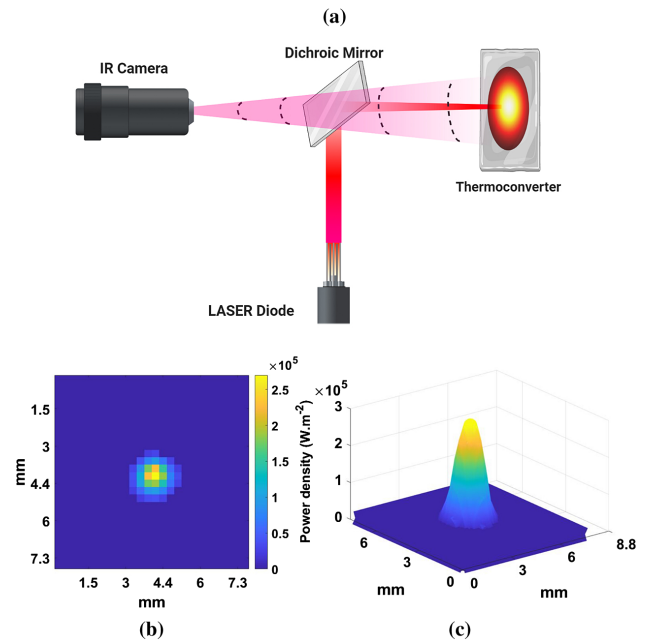


**Fig. 9.** (a) Experimental setup, (b) image of the estimated source, and (c) surface of the estimated source.

where  $S_{\text{pixel}}$  is the area of one pixel with a value of  $8 \times 10^{-8} \text{ m}^2$ . The estimation represents a relative error of 0.45%.

## B. Contactless Application for Different Optical Sources

In this section, the use of our appliance as a power meter is demonstrated.

### 1. Near-IR Laser Source

In this first application, a NIR laser diode ( $\lambda = 980 \text{ nm}$ ) with a power of  $P = 280 \text{ mW}$  is used as an excitation source. The time of the square-shaped pulse is 40 ms. A dichroic mirror is placed between the IR camera and the thermoconverter, as shown in Fig. 9, and enabled to reach the temperature of the thermoconverter at the front side. As the thermoconverter is a thermally thin body, the temperature at the front side is equal to the temperature at the back side (no temperature gradient along the thermoconverter thickness). The thermoconverter is placed at a distance of 40 cm from the IR camera.

Figures 9(b) and 9(c) show the reconstruction of the spatial distribution and energy density of the source after inversion. The diameter of the spot after the flux estimation is equal to 3 mm, which is in agreement with the optical considerations. The estimated convective exchange coefficient is  $h = 31 \text{ W} \cdot \text{m}^{-2} \cdot \text{K}^{-1}$ . This value is very large compared to that estimated for the Joule heated resistance. This is due in small part to the fact that the thermoconverter is not insulated and in large part to the fact that the average temperature of the thermoconverter is very high (4 K at  $t = 33 \text{ ms}$ ). The power estimated using Eq. (13) was found to be  $285.3 \pm 3.7 \text{ mW}$  with a relative error of 1.9%.

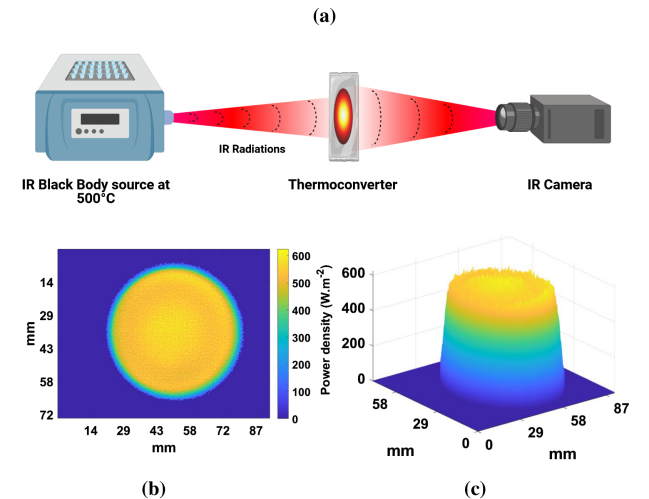


**Fig. 10.** (a) Experimental setup, (b) image of the estimated source, and (c) surface of the estimated source.

### 2. IR Blackbody Source

In this second application case, the source used comes from an IR blackbody (BBSH) from Prisma instruments, whose emissivity is estimated to have an uncertainty of 0.5% to  $\epsilon_{\text{BB}} = 0.98$ . The blackbody temperature is adjustable in the range [500°C; 1200°C]. In our case, the blackbody temperature is set to  $T_{\text{BB}} = 500^\circ\text{C}$  [see Fig. 10(a)]. A square-shaped pulse of 4.5 s is applied using a chopper synchronized with the IR camera.

Figures 10(b) and 10(c) show the reconstruction of the spatial distribution and power density of the source after inversion. The thermoconverter is placed at a distance of 10 cm from the blackbody. The diameter of the blackbody nozzle is 43 mm. The spatial analysis of the estimated flux shows that the beam has a diameter of 60 mm, which represents a beam

401

402

403

404

405

406

407

408

409

410

411

412

413

414

415 divergence of  $5^\circ$ . The estimated convective exchange coefficient  
 416 is  $b = 17 \text{ W} \cdot \text{m}^{-2} \cdot \text{K}^{-1}$ . This value is lower than that  
 417 in the NIR laser case because the average temperature of the  
 418 thermoconverter is also lower (2.5 K at  $t = 1$  s).

419 The power estimated using Eq. (13) is  $1.357 \pm 0.015 \text{ W}$ . To  
 420 validate the value of the estimated flux, a short calculation based  
 421 on the Stefan–Boltzman law and the notion of the form factor  
 422 in thermal radiation to allow modeling the radiative exchanges  
 423 between two black disks ( $\varepsilon \approx 1$ ) separated by a perfectly trans-  
 424 parent medium is performed. This calculation predicts that  
 425 the thermoconverter should theoretically receive a flux of  
 426  $P = 1.15 \text{ W}$  and shows that the estimated flux is in the order of  
 427 the magnitude of the expected power with a relative error equal  
 428 to 15.25%.

### 429 3. Gigahertz Source

430 In this third application case, a Terasense gigahertz source  
 431 ( $f = 100 \text{ GHz}$ ,  $\lambda = 3 \text{ mm}$ ) with a power of  $P = 400 \text{ mW}$  is  
 432 used, and the absorbance ( $\mathcal{A}$ ) of the thermoconverter in this  
 433 wave is equal to 61% [9]. The thermoconverter is placed at a  
 434 distance of 5 cm from the source. The gigahertz source is syn-  
 435 chronized with a waveform generator that allows delivery of a  
 436 square-shaped pulse of 1.25 s.

437 The estimated convective exchange coefficient is  
 438  $b = 20.24 \text{ W} \cdot \text{m}^{-2} \cdot \text{K}^{-1}$ . This value is higher than that in  
 439 the blackbody case and lower than that in the NIR laser case.  
 440 This is related to the value of the average temperature of the  
 441 thermoconverter, which is between those of the two cases (6 K  
 442 at  $t = 1$  s). Figures 11(b) and 11(c) show the reconstruction  
 443 of the spatial distribution and power density of the source  
 444 after inversion. In this case, the source power is estimated by  
 445 modifying Eq. (13) to take into account the absorbance of the  
 446 thermoconverter at the emission wavelength of the source as  
 447 follows:

$$P_{\text{estimated}} = \left( \iint \mathcal{Y}(x, y) \right) \times S_{\text{pixel}} \times \frac{1}{\mathcal{A}}. \quad (14)$$

448 The power estimated using Eq. (14) is  $404.8 \pm 5 \text{ mW}$  with a  
 449 relative error equal to 1.19%.

### 450 4. Radio-Frequency Source

451 In this fourth application case, an ultra-high-frequency (UHF)  
 452 radio wave antenna source ( $f = 500 \text{ Mhz}$ ,  $\lambda = 0.6 \text{ m}$ ) in an  
 453 anechoic chamber is used. The thermoconverter used has a sur-  
 454 face area of  $1 \text{ m}^2$ , and it is placed at a distance of 1 cm from  
 455 the source. The power delivered by the source and the absorbance  
 456 of the thermoconverter at this wavelength are unknown, so the  
 457 estimated flux is proportional to the absorbance of the thermo-  
 458 converter. Figures 12(b) and 12(c) show the reconstruction of  
 459 the spatial distribution and power density of the source after  
 460 inversion. The estimated convective exchange coefficient is  
 461  $b = 10.14 \text{ W} \cdot \text{m}^{-2} \cdot \text{K}^{-1}$ . This value is the lowest of the con-  
 462 vective exchange coefficient values estimated for the optical  
 463 sources (except for the joule heat resistance). This is because the  
 464 average temperature of the thermoconverter is lower than that  
 465 in the previous cases [34] (1.3 K at  $t = 1$  s). The power of the  
 466 source estimated using Eq. (14) is  $6.5 \pm 0.17 \times \frac{1}{\mathcal{A}} \text{ W}$ . This

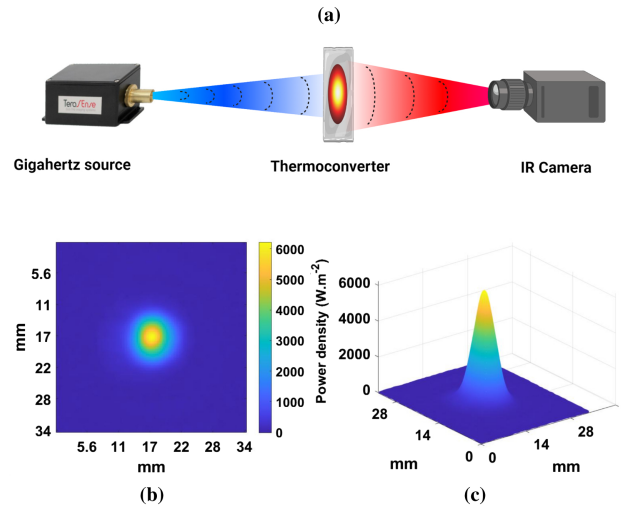


Fig. 11. (a) Experimental setup, (b) image of the estimated source, and (c) surface of the estimated source.

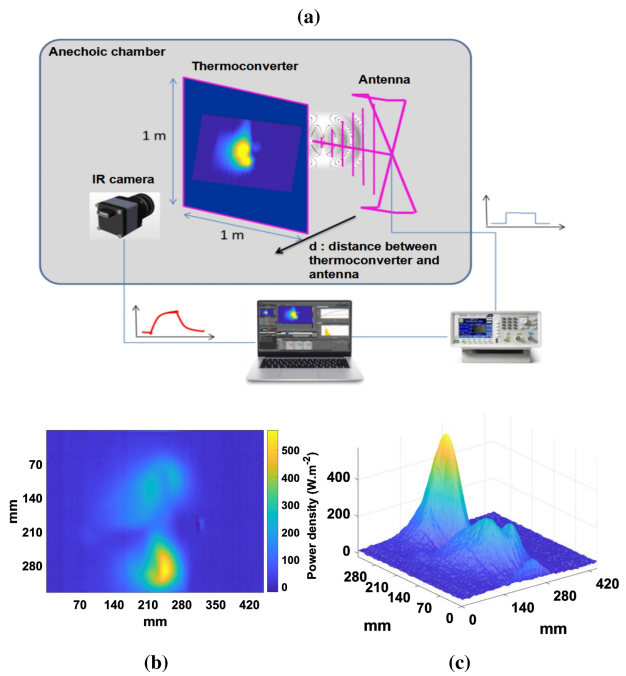


Fig. 12. (a) Experimental setup, (b) image of the estimated source, and (c) surface of the estimated source.

467 result is presented to demonstrate the hyperspectral aspect of the  
 468 thermoconverter, on the one hand, and to highlight the need to  
 469 know the absorbance of the thermoconverter (at the emission  
 470 wavelength of the source) to estimate the power of the source, on  
 471 the other hand.

### 472 C. Performances of the Sensor

473 The performances of the flux sensor are described here. It should  
 474 be remembered that the sensor is the result of a coupled con-  
 475 figuration thermoconverter-IR camera. Consequently, the  
 476 performances of the sensor are linked and limited, on the one  
 477 hand, by the characteristics of the camera ( $25 \mu\text{m} \times 25 \mu\text{m}$ )

**Table 3. Performances of the Flux Sensor**

	Joule Effect by Resistance	NIR Laser Source	IR Blackbody Source	Gigahertz Source	Radio-Frequency Source
Spatial resolution ( $\mu\text{m}^2$ )	$283 \times 283$	$180 \times 180$	$290 \times 290$	$280 \times 280$	$1400 \times 1400$
sensitivity ( $\mu\text{W}/\text{m}^2$ )			$\frac{1.815 \times \text{TI}(\mu\text{s})}{A}$		

pitch size, minimum sensitivity of 20 mK, and variable according to the integration time), and, on the other hand, by the photothermal effect within the thermoconverter (absorbance, diffusion of the heat, and inversion of the heat transfer). The calculated spatial resolution varies depending on the sensor application due to the change in the thermoconverter-IR camera configuration in each case (size of the thermoconverter used, distance between the thermoconverter and the IR camera). The sensitivity of the sensor is given in the form of a general formula that takes into account the limits of the thermoconverter-IR camera configuration, the integration time of the camera, and the absorbance of the thermoconverter at the source wavelength.

## 6. CONCLUSION

A hyperspectral flux sensor using a thermoconverter to estimate the spatial distribution of a source and its flux density has been developed.

The most important point is the experimental validation of the thermoconverter and IR camera configuration. First, the development of a thermal model to precisely characterize the heat transfer within the thermoconverter was described. Then, a first inverse method was used to estimate the heat losses to increase the model's robustness and precision. Finally, a second inverse method allowed the spatial reconstruction of sources and their flux density.

The methodology was validated on a joule heated resistor, presented here as the reference. To illustrate the ultra-broadband quality of the technique, examples of applications with several sources have been discussed: (i) a NIR laser source, (ii) an IR blackbody source, (iii) a gigahertz source, and (iv) a UHF radio-frequency antenna.

This research offers new perspectives in the fields of hyperspectral fluxmetry and thermal inverse methods, with many applications projected in the fields of optical applications, building science, and industries.

**Funding.** Centre National de la Recherche Scientifique.

**Acknowledgment.** This research is part of the IGAR project that aims to thermally and chemically characterize plasma torches. The main challenge is the non-contact 3D temperature and flux field measurement for energy optimization of these torches. The authors thank ADEME for the support of this work through the IGAR project with Arcelor-Mittal.

**Disclosures.** The authors declare no conflicts of interest.

**Data Availability.** Data underlying the results presented in this paper are not publicly available at this time but may be obtained from the authors upon reasonable request.

## REFERENCES

1. D. Jaeggi, H. Baltès, and D. Moser, "Thermoelectric ac power sensor by CMOS technology," *IEEE Electron Device Lett.* **13**, 366–368 (1992).

2. J. C. Johnson and G. A. Massey, "Bolometric laser power meter for sensitive measurements in the IR–vacuum UV spectral range," *Appl. Opt.* **17**, 2268–2269 (1978).
3. G. E. Mohler, "Laser power meter," (1975).
4. G. A. Rex, "Laser power-energy meter," (1971).
5. C. Pradere, J. Caumes, D. Balageas, S. Salort, E. Abraham, B. Chassagne, and J. Batsale, "Photothermal converters for quantitative 2D and 3D real-time terahertz imaging," *Quant. InfraRed Thermogr. J.* **7**, 217–235 (2010).
6. R. Müller, W. Bohmeyer, M. Kehrt, K. Lange, C. Monte, and A. Steiger, "Novel detectors for traceable THz power measurements," *J. Infrared Millim. Terahertz Waves* **35**, 659–670 (2014).
7. W. Flores-Fuentes, J. E. Miranda-Vega, M. Rivas-López, O. Sergiyenko, J. C. Rodríguez-Quiñonez, and L. Lindner, "Comparison between different types of sensors used in the real operational environment based on optical scanning system," *Sensors* **18**, 1684 (2018).
8. D. L. Balageas, P. Levesque, and A. A. Deom, "Characterization of electromagnetic fields using a lock-in infrared thermographic system," *Proc. SPIE* **1933**, 274–285 (1993).
9. M. Romano, A. Chulkov, A. Sommier, D. Balageas, V. Vavilov, J. Batsale, and C. Pradere, "Broadband sub-terahertz camera based on photothermal conversion and IR thermography," *J. Infrared Millim. Terahertz Waves* **37**, 448–461 (2016).
10. H. Gidik, D. Dupont, and G. Bedek, "Development of a radiative heat fluxmeter with a textile substrate," *Sens. Actuators A* **271**, 162–167 (2018).
11. C. Jim and H. He, "Estimating heat flux transmission of vertical greenery ecosystem," *Ecol. Eng.* **37**, 1112–1122 (2011).
12. K. Yang and J. Wang, "A temperature prediction-correction method for estimating surface soil heat flux from soil temperature and moisture data," *Sci. China D* **51**, 721–729 (2008).
13. J. Gardarein, J. Battaglia, S. Lohle, P. Jullien, B. Van Ootegem, J. Couzi, and J. Lasserre, "Miniaturized heat flux sensor for high enthalpy plasma flow characterization," *Inverse Probl. Sci. Eng.* **21**, 1–14 (2013).
14. A. Zribi, M. Barthès, S. Bégot, F. Lanzetta, J. Rauch, and V. Moutarlier, "Design, fabrication and characterization of thin film resistances for heat flux sensing application," *Sens. Actuators A* **245**, 26–39 (2016).
15. M. Groz, E. Abisset-Chavanne, A. Meziane, A. Sommier, and C. Pradere, "Bayesian inference for 3D volumetric heat sources reconstruction from surfacic IR imaging," *Appl. Sci.* **10**, 1607 (2020).
16. M. Groz, E. Abisset-Chavanne, A. Meziane, A. Sommier, and C. Pradere, "Three-dimensional reconstruction of thermal volumetric sources from surface temperature fields measured by infrared thermography," *Appl. Sci.* **9**, 5464 (2019).
17. P. Burgholzer, M. Thor, J. Gruber, and G. Mayr, "Three-dimensional thermographic imaging using a virtual wave concept," *J. Appl. Phys.* **121**, 105102 (2017).
18. S. Waters, P. Burgholzer, A. Mendioroz, and I. S. de Ocariz, "3D reconstruction of tilted cracks using infrared thermography and the virtual wave concept," *14th International Conference on Quantitative Infrared Thermography*, Berlin, Germany (2018), pp. 25–29.
19. D. Nortershauser and P. Millan, "Resolution of a three-dimensional unsteady inverse problem by sequential method using parameter reduction and infrared thermography measurements," *Numer. Heat Transfer* **37**, 587–611 (2000).
20. D. Nortershauser and P. Millan, "Estimation of moving heat sources with a three-dimensional unsteady inverse method," *Aerosp. Sci. Technol.* **5**, 529–540 (2001).
21. E. Badine, M. Bardoux, N. Abboud, M. Depriester, S. Longuemart, Z. Herro, and A. H. Sahraoui, "Thermoreflectance profile analysis and multiparameter 3D fitting model applied to the measurement

- 589 of thermal parameters of thin film materials," *J. Phys. D* **52**, 205303  
590 (2019). 609
- 591 22. D. Maillet, S. André, J.-C. Batsale, A. Degiovanni, and C. Moyne, 610  
592 *Thermal Quadrupoles, Solving the Heat Equation Through Integral* 611  
593 *Transforms* (Wiley-Blackwell, 2000). 612
- 594 23. J. Pailhes, C. Pradere, J.-L. Battaglia, J. Toutain, A. Kusiak, A. W. 613  
595 Aregba, and J.-C. Batsale, "Thermal quadrupole method with internal 614  
596 heat sources," *Int. J. Thermal Sci.* **53**, 49–55 (2012). 615
- 597 24. J. Toutain, J. Battaglia, C. Pradere, J. Pailhes, A. Kusiak, W. Aregba, 616  
598 and J. Batsale, "Numerical inversion of Laplace transform for time 617  
599 resolved thermal characterization experiment," *J. Heat Transfer* **133**, 618  
600 044504 (2011). 619
- 601 25. L. Gaverina, J. Batsale, A. Sommier, and C. Pradere, "Pulsed flying 620  
602 spot with the logarithmic parabolas method for the estimation of 621  
603 in-plane thermal diffusivity fields on heterogeneous and anisotropic 622  
604 materials," *J. Appl. Phys.* **121**, 115105 (2017). 623
- 605 26. F. White, *Heat and Mass Transfer*, Series in Mechanical Engineering 624  
606 (Addison-Wesley, 1988). 625
- 607 27. J. Hadamard, *Lectures on Cauchy's Problem in Linear Partial* 626  
608 *Differential Equations* (Yale University, 1923).
28. A. Tikhonov, "On the solution of ill-posed problems and the method 609  
of regularization," *Russ. Acad. Sci.* **151**, 501–504 (1963). 610
29. R. Gray, "Toeplitz and circulant matrices: a review," *Found. Trends* 611  
*Commun. Inf. Theory* **2**, 155–239 (2006). 612
30. E. Picard, "Sur un theoreme general relatif aux equations integrales 613  
de premiere espece et sur quelques problemes de physique mathe- 614  
matique," *Rend. Circ. Mate. Palermo* **29**, 79–97 (2010). 615
31. J. A. Nelder and R. Mead, "A simplex method for function minimiza- 616  
tion," *Comput. J.* **7**, 308–313 (1965). 617
32. N. S. Bondareva, M. Sheikholeslami, and M. A. Sheremet, "The influ- 618  
ence of external temperature and convective heat exchange with an 619  
environment on heat transfer inside phase change material embed- 620  
ded brick," *J. Energy Storage* **33**, 102087 (2021). 621
33. E. Placido, M. Arduini-Schuster, and J. Kuhn, "Thermal properties 622  
predictive model for insulating foams," *Infrared Phys. Technol.* **46**, 623  
219–231 (2005). 624
34. J.-W. Wu, W.-F. Sung, and H.-S. Chu, "Thermal conductivity of poly- 625  
urethane foams," *Int. J. Heat Mass Transfer* **42**, 2211–2217 (1999). 626